The effect of Duffing-type nonlinearities and Coulomb damping on the response of an energy harvester to random excitations

P L Green[1], K Worden[2], K Atallah[3], N D Sims[4]

[1] Mr. Peter L Green
Department of Mechanical Engineering, University of Sheffield, Mappin Street, Sheffield, United Kingdom, S1 3JD
Tel: 07867673881
Email: mep09plg@shef.ac.uk

[2] Professor Keith Worden
Department of Mechanical Engineering, University of Sheffield, Mappin Street, Sheffield, United Kingdom, S1 3JD
Tel:+44 (0)114 222 7758
Email: K.Worden@sheffield.ac.uk

[3] Dr. Kais Atallah
Department of Electrical Engineering, University of Sheffield, Mappin Street, Sheffield, United Kingdom, S1 3JD
Tel:+44 (0) 114 222 5812
Email: k.atallah@sheffield.ac.uk

[4] Dr. Neil D Sims
Department of Mechanical Engineering, University of Sheffield, Mappin Street, Sheffield, United Kingdom, S1 3JD
Tel:+44(0)114 222 7724
Email: n.sims@sheffield.ac.uk

ABSTRACT

Linear energy harvesters can only produce useful amounts of power when excited close to their natural frequency. Due to the uncertain nature of ambient vibrations it has been hypothesised that such devices will perform poorly in real world applications. To improve performance, it has been suggested that the introduction of nonlinearities into such devices may extend the bandwidth over which they perform effectively. In this work a magnetic levitation device with nonlinearities similar to the Duffing oscillator is considered. The governing equations of the device are formed in which the effects of friction are considered. Analytical solutions are used to explore the effect that friction can have on the system when it is under harmonic excitations. Following this, a numerical model is formed. A differential evolution algorithm is used alongside experimental data to identify the relevant parameters of the device. The model is then validated using experimental data. Monte Carlo simulations are then used to analyse the effect of coulomb damping and Duffing-type nonlinearities when the device is subjected to broadband white noise and coloured noise excitations.

1 INTRODUCTION

The concept of harvesting electrical energy from mechanical vibrations and using it to drive low-power systems has received much attention in recent years. Williams and Yates (1996) investigated the feasibility of harvesting electrical energy from bridge vibrations, with the aim of using it to power microelectromechanical systems (MEMS). In their work a device was proposed which consisted of a magnet, attached to a spring, and surrounded by a coil of wire. The device was designed such that the vibrations of the bridge would cause the magnet to oscillate within the coil and generate a voltage via electromagnetic induction. The system was modeled as a simple mass-spring-damper where the damper was used to model the electromagnetic transducer.

In work following this, the response of the device to a sinusoidal excitation was analysed in more detail (Stephen, 2006; Beeby, Tudor, and White, 2006). A resounding conclusion was that, when excited by a sinusoidal excitation, the device was only able to produce useful amounts of power when excited close to its natural frequency. As the dominant frequencies of most environmental excitations usually take place over a large bandwidth or are time dependent, it can be concluded that energy harvesters that only operate well near resonance will be poorly suited to real world applications. To solve this problem two main solutions have been proposed:

- increasing the bandwidth over which the device can produce useful amounts of energy,
- designing energy harvesters which can adapt their natural frequency to match that of the excitation frequency.

Reviews of attempts to apply these solutions to a range of energy harvesting devices can be found in (Zhu, Tudor, and Beeby, 2010; Tang, Yang, and Soh, 2010). As well as this, devices have been proposed which are designed to be able to harvest useful amounts of energy from multiple frequencies simultaneously (Yang et al., 2009).

Mann and Sims (2009) proposed a single-degree of freedom device which relied on magnetic levitation rather than linear springs. A schematic diagram of the device and its corresponding circuit diagram are shown in FIGURES 1(a) and (b) respectively. It was shown that the governing equations of the device contained a cubic stiffness term - similar to that of the Duffing oscillator. The effect of this nonlinearity was to 'skew' the frequency response curve of the device. It was hypothesised that the introduction of this nonlinearity may extend the bandwidth over which the device could produce useful amounts of power.

Subsequently, in (Daqaq, 2010, 2011) a device similar to that proposed by Mann and Sims was considered, the only difference being that its orientation had been changed by ninety degrees. This had the effect of removing gravity from the governing equations of the device. The Fokker-Planck-Kolmogorov equation was used to analyse how it responded to different types of random excitation. In these works, a white noise force was applied both to the centre magnet (Daqaq, 2010) and the base of the device (Daqaq, 2011). It was concluded, in both cases, that the addition of the nonlinearity did not affect the potential power output of the device.

In the present study, experimental tests are conducted using an upright magnetic levitation device. The governing equations of the device are derived, which differs from previous work in that the effect of friction is also considered. A self adaptive differential evolution algorithm is then used alongside experimental data to identify the parameters needed in the model. Subsequent simulations show an excellent agreement between the response of the model and that of the experiment in both the time and frequency domains. Once validated, the model is used to produce dimensionless contour plots detailing the effect that different levels of nonlinearity, electromagnetic coupling and coulomb damping can have on the system when the base of the device is subjected to white noise and coloured base accelerations.

At this stage it should be emphasised that the aim of the present experiments was not to harvest power but rather to understand and validate the theoretical power harvesting potential. For this reason the experiment did not include an electromagnetic coupling and the associated electrical energy storage or dissipation

systems. Instead the energy dissipated is due to viscous friction, and a dimensionless approach enables understanding of how energy capture could be achieved by the addition of more damping through electromagnetic coupling.

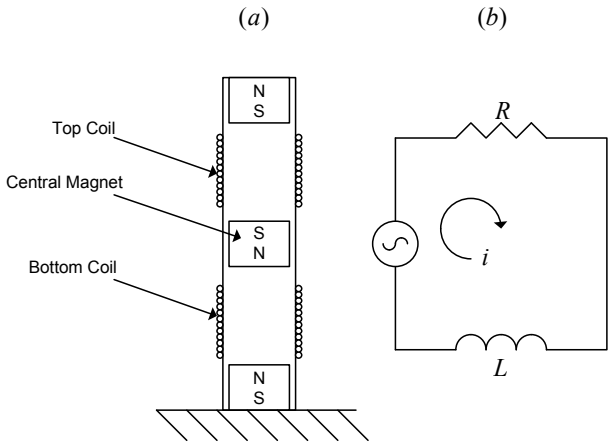

Figure 1: (a) Schematic diagram and (b) circuit diagram of the magnetic levitation energy harvester proposed by Mann and Sims.

2 MODEL FORMULATION

In this section, the mechanical and electrical governing equations of the device are derived.

2.1 Equation of Motion

A schematic diagram of the model is shown in FIGURE 2 where the spring represents the magnetic restoring force, the dashpot represents a combination of coulomb and viscous damping, and x and y represent the centre magnet and base displacements respectively. The equation of motion for this system can be written as:

$$-m\ddot{x} = c(\dot{x} - \dot{y}) + k(x - y) + k_3(x - y)^3 + F_d sgn(\dot{x} - \dot{y}) + mg, \tag{1}$$

where m represents the mass of the centre magnet, g is the acceleration due to gravity, k is the linear stiffness, k_3 the cubic stiffness, c the viscous damping, F_d the coulomb damping coefficient and

$$sgn(\dot{x} - \dot{y}) = \begin{cases} 1, & \dot{x} - \dot{y} > 0 \\ 0, & \dot{x} - \dot{y} = 0 \\ -1, & \dot{x} - \dot{y} < 0 \end{cases} \tag{2}$$

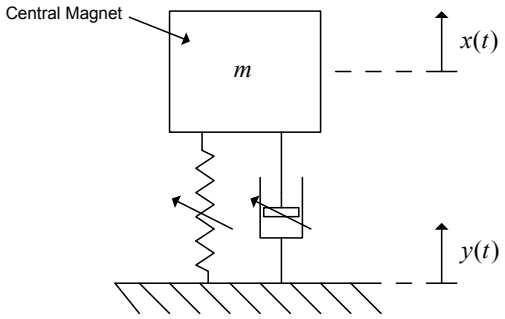

Figure 2: Energy harvester model.

It should be noted here that the magnetic restoring forces have been modelled as a third order polynomial (following the work of Mann and Sims (2009)). In practice, dipole, distributed or point charge magnet models are available (Sneller and Mann (2010)). However, it will be shown in Section 6 that a high fidelity model can be obtained with the addition of a cubic nonlinearity spring force.

By setting $X_1 = x$ and $X_2 = \dot{x}$, EQUATION 1 can be put in state space form:

$$\dot{X_1} = X_2, \tag{3}$$

$$\dot{X_2} = \frac{-mg - c(X_2 - \dot{y}) - k(X_1 - y) - k_3(X_1 - y)^3 - F_d sgn(X_1 - y)}{m}. \tag{4}$$

To perform a time domain simulation, the solutions of EQUATIONS 3 and 4 were obtained numerically using the fourth-order Runge-Kutta method.

2.2 Electromagnetic Transducer

This section is concerned with simplified modelling of the electromagnetic transducer that would be present in a practical energy harvester. A more detailed discussion of different transducer configurations can be found in Mitcheson et al. (2004). In this analysis it is assumed that the magnetic flux density does not change over the regions we are interested in.

Faraday's law states that the voltage induced in the circuit will be proportional to the relative velocity of the magnet:

$$V(t) = Bl\dot{z}(t), \tag{5}$$

where V is the induced voltage, B is the magnetic flux density, l is the length of the coiled wire and $\dot{z}$ is the relative velocity between the centre magnet and the base of the device $\dot{z} = \dot{y} - \dot{x}$. Furthermore, Lorenz's law states that the force exerted on the magnet as a result of inducing the voltage is given by:

$$F(t) = Bi(t)l, \tag{6}$$

where i represents current. Finally, recalling that the circuit contains a resistor and an inductor (as shown in FIGURE 1(b)) then the induced voltage can also be expressed as:

$$V(t) = i(t)R + \frac{di(t)}{dt}L, \tag{7}$$

where R is the combination of coil and load resistances and L is the coil inductance. Taking Laplace transforms (assuming zero initial conditions) and combining EQUATIONS 5, 6 and 7, the following expression can be obtained:

$$\mathcal{L}(F(t)) = \frac{s(Bl)^2\mathcal{L}(z(t))}{R + sL}, \tag{8}$$

where s is the Laplace operator and $\mathcal{L}$ is the Laplace transform. If it is assumed that the inductance is small compared to the resistance then the transducer can be modeled as a viscous damper where:

$$c = \frac{(Bl)^2}{R}. \tag{9}$$

Assuming that the viscous damping in the system is only due to the electromagnetic coupling, then the power available for harvest is given by:

$$P = c|\dot{z}|^2. \tag{10}$$

A detailed analysis of the effect of coil inductance can be found in Mann and Sims (2010). Once again it should be noted that this work is concerned with maximising the kinetic energy available within the device which could, potentially, be converted into electrical energy using an electromagnet coupling. It does not discuss the difficulties which may arise if were one were to consider the issues of energy capture and storage.

3 ANALYTICAL SOLUTION

To gain more insight into the behavior of the system, the method of harmonic balance was used to approximate the power output of the device when under a sinusoidal base excitation.

3.1 Frequency Response

Neglecting DC components, the equation of motion of the device can be written as:

$$m\ddot{z} + c\dot{z} + F_d sgn(\dot{z}) + kz + k_3 z^3 = -m\ddot{y}, \tag{11}$$

where $z = (x - y)$. Setting the input as:

$$y = Y sin(\omega t + \phi), \tag{12}$$

it is assumed that the response of the system is dominated by the first harmonic:

$$z = Z sin(\omega t). \tag{13}$$

Note that the phase term (ϕ) has been transferred to the input y as it helps to simplify matters later. Taking EQUATION 12, differentiating twice and rewriting using elementary trigonometric relations one finds that:

$$\ddot{y} = -m\omega^2 Y(sin(\omega t)cos(\phi) + cos(\omega t)sin(\phi)). \tag{14}$$

Inserting EQUATIONS 12 and 13 into EQUATION 11 one obtains:

$$\begin{aligned} -m\omega^2 Z sin(\omega t) + c\omega Z cos(\omega t) + kZ sin(\omega t) + k_3 Z^3 sin^3(\omega t) + \\ F_d sgn(cos(\omega t)) = m\omega^2 Y(sin(\omega t)cos(\phi) + cos(\omega t)sin(\phi)). \end{aligned} \tag{15}$$

The coefficient of F_d was then expanded up to the first harmonic using the Fourier series:

$$\begin{aligned} sgn(cos(\omega t)) &= \frac{4}{\pi}cos(\omega t) - \frac{4}{3\pi}cos(3\omega t) + \frac{4}{5\pi}cos(5\omega t) - ... \\ &\approx \frac{4}{\pi}cos(\omega t). \end{aligned} \tag{16}$$

The coefficient of k_3 was then expanded using elementary trigonometric relations (again, only up to the first harmonic):

$$Z^3 sin^3(\omega t) = Z^3\left(-\frac{1}{4}sin(3\omega t) + \frac{3}{4}sin(\omega t)\right) \approx Z^3\frac{3}{4}sin(\omega t). \tag{17}$$

Consequently, EQUATION 15 becomes:

$$-m\omega^2 Z sin(\omega t) + c\omega Z cos(\omega t) + kZ sin(\omega t) + k_3 Z^3\left(\frac{3}{4}sin(\omega t)\right) + \tag{18}$$

$$\frac{4F_d}{\pi}cos(\omega t) = m\omega^2 Y(sin(\omega t)cos(\phi) + cos(\omega t)sin(\phi)). \tag{19}$$

Equating coefficients of $sin(\omega t)$ and $cos(\omega t)$ one obtains two equations:

$$-m\omega^2 Z + kZ + \frac{3}{4}k_3 Z^3 = m\omega^2 Y cos(\phi), \tag{20}$$

$$c\omega Z + \frac{4}{\pi}F_d = m\omega^2 Y sin(\phi). \tag{21}$$

Squaring and summing EQUATIONS 20 and 21 one can eliminate the phase term and find that:

$$\left(-m\omega^2 Z + kZ + \frac{3k_3 Z^3}{4}\right)^2 + \left(c\omega Z + \frac{4F_d}{\pi}\right)^2 = m^2\omega^4 Y^2. \tag{22}$$

After manipulation, if was found that Z could be obtained by finding the roots of a sixth order polynomial:

$$Z^6\left(\frac{9k_3^2}{16}\right)+Z^4\left(-\frac{3}{2}m\omega^2k_3+\frac{3}{2}kk_3\right)+Z^2(m^2\omega^4-2m\omega^2k+k^2+c^2\omega^2)$$
$$Z\left(\frac{8c\omega F_d}{\pi}\right)+\left(\frac{16F_d^2}{\pi^2}-m^2\omega^4Y^2\right)=0. \tag{23}$$

The solutions to EQUATION 23 were found using the Matlab *roots* command (MathWorks., 2004). Once Z was obtained the negative and imaginary solutions were neglected as being unphysical. The power output of the device was found using the relation:

$$P=(\omega Z)^2c. \tag{24}$$

To validate the analytical result, the model detailed in Section 2 was used to analyse the frequency response of the device. To achieve this, the model was subjected to a sinusoidal excitation and the resulting power output was monitored as the excitation frequency was stepped up or down. FIGURE 3 shows that there was a reasonably good match between the analytical and simulation results.

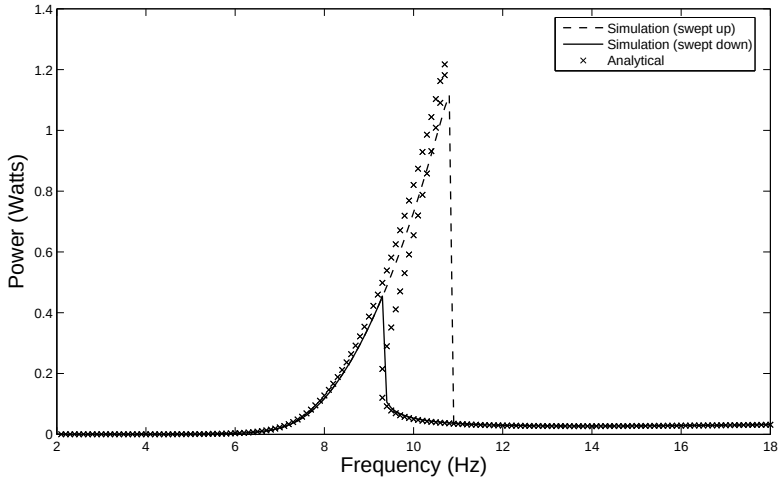

Figure 3: Power output of device at different frequencies where $m = 0.02$ kg, $k = 50$ N/m, $k_3 = 20000$ N/m^3, $c = 0.1$ Ns/m, $F_d = 0.01$ N, $Y = 4$mm and $g = 9.81$m/s^2. Crosses represent the analytical solutions (equation 23) while dashed and solid lines represent swept up and swept down simulation results respectively. Exciting the model with a stepped-sine wave, the forth order Runge-Kutta method was used to numerically solve equations 3 and 4 thus obtaining the frequency response of the device.

3.2 The Effect of Friction

The analysis shown above is based on the assumption that there is relative motion between the centre magnet and base of the device. Consequently, this approach is only valid if:

$$|c\dot{z}+kz+k_3z^3+m\ddot{y}|>|F_dsgn(\dot{z})|, \tag{25}$$

such that the forces acting on the mass are large enough to overcome the friction in the system. As a result, the frequency where the device starts to move relative to the base (termed the slipping frequency) is when:

$$|c\dot{z}+kz+k_3z^3+m\ddot{y}|=|F_dsgn(\dot{z})|. \tag{26}$$

Applying the same procedure as shown in the previous section allows this to be written as:

$$\left(kZ + \frac{3}{4}k_3Z^3\right)^2 \left(\omega Zc + \frac{4}{\pi}F_d\right)^2 = m^2\omega^4Y^2, \tag{27}$$

where Z changes with ω according to EQUATION 23. The value of ω that satisfies EQUATION 27 will be the slipping frequency. FIGURE 4 shows the swept up frequency response of the model (using the same techniques as the previous section) and shows that, when excited sinusoidally, EQUATIONS 23 and 27 can be used to predict the frequency where the device moves from stick to slip behavior with a reasonable degree of accuracy. In FIGURE 4 (c) one can see that the increase in friction has decreased the effect of the nonlinear spring to the point where the jump phenomenon has been removed from the frequency response of the device. The same effect would occur is one was to increase the viscous damping present in the system. It remains to be seen how friction and Duffing-type nonlinearities influence the behavior of the device when it is under a random excitation. This will be the focus of the remaining sections.

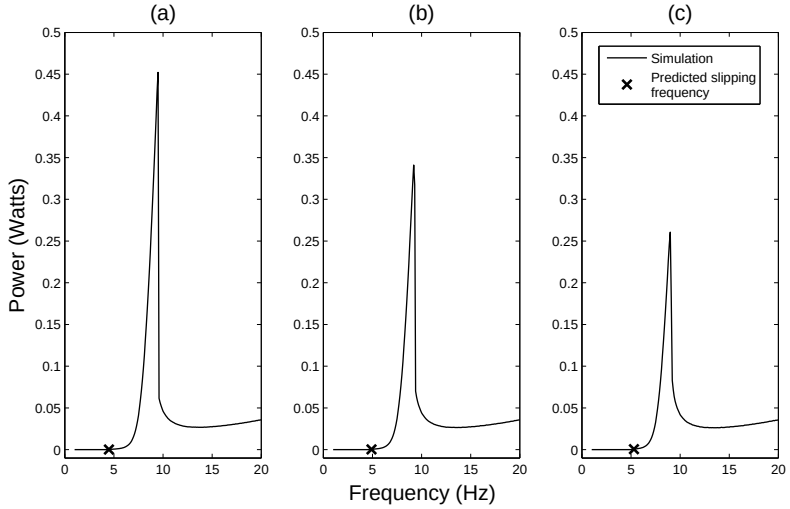

Figure 4: Power output of device at different frequencies where $m = 0.02$ kg, $c = 0.1$ N/s, $k = 50$ N/m, $k_3 =$ N/m^3, $Y = 0.004$ m and $F_d =$ (a) 0.05, (b) 0.06, (c) 0.07 N. Exciting the model with a stepped-sine wave, the forth order Runge-Kutta method was used to numerically solve equations 3 and 4 thus obtaining the frequency response of the device.

4 EXPERIMENTAL APPARATUS

A diagram of the experimental apparatus is shown in FIGURE 5. The top and bottom magnets were both attached to an aluminium rod which was, in turn, bolted to an electromagnetic shaker via an aluminium extension piece. The extension piece was used to keep the device away from the magnetic effects of the shaker. A linear variable differential transformer (LVDT) was screwed into the aluminium rod, allowing it to measure the displacement of the shaker table.

The centre magnet was able to move up and down the aluminium rod via two sets of linear bearings. A plastic penny washer was glued to the magnet such that the displacement of the centre magnet could be measured using a laser triangulation sensor.

In Section 2.2 it was shown that the electrical damping introduced by an electromagnetic coupling could be modelled as viscous damping such that the total damping in the system is given by:

$$c_{total} = c_m + c_e, \tag{28}$$

where c_m and c_e represent the mechanical and viscous damping terms respectively. As a result, the device shown in FIGURE 5 could be used to validate the model even though all the damping was mechanical and no coupling was present.

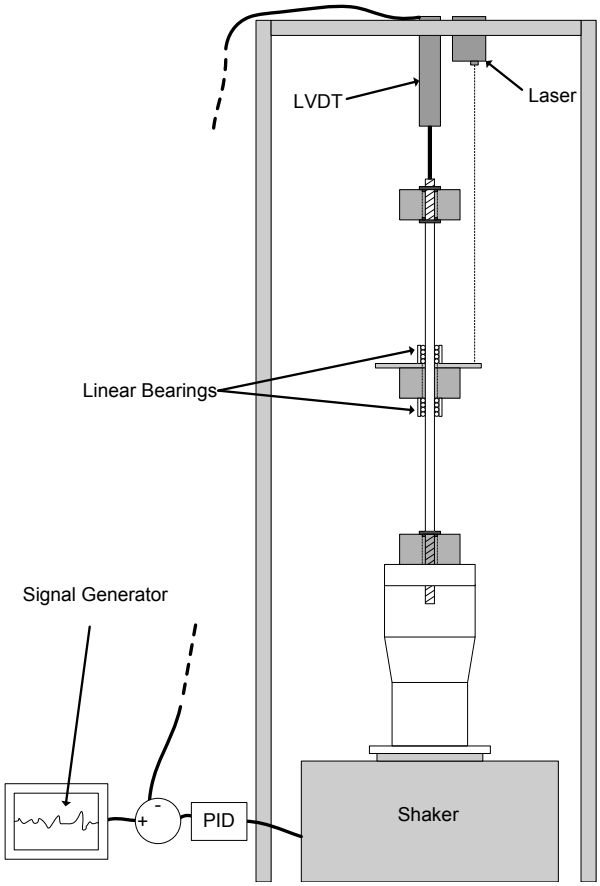

Figure 5: Experimental apparatus.

To achieve the desired excitation a proportional-integral-derivative (PID) controller was used with the LVDT to control the position of the shaker table. FIGURE 6 shows how the addition of the controller improved the ability of the shaker to follow a square wave input.

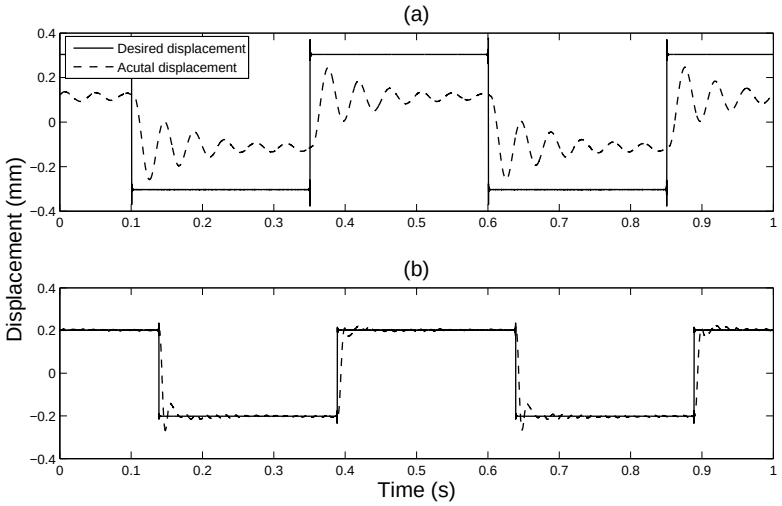

Figure 6: Response of the shaker to a square wave input with (a) open loop and (b) closed loop PID control. Solid and dashed lines represent desired and actual displacements respectively.

The aim of the experiment was to excite the base of the energy harvester with a random, white noise, force. In reality a white noise signal cannot be achieved experimentally as the bandwidth of the noise is limited by the fundamental sample frequency of the system and the actuator dynamics. A Gaussian, band-limited white noise signal was created, integrated twice and then filtered to remove integral drift as well as unwanted higher frequencies before being sent to the shaker. This is shown in block diagram form in FIGURE 7.
Upon studying the frequency response of the energy harvesting device it was found to have a natural frequency of approximately 8.5 Hz. As a result it was ensured that the force applied to the base of the device had a flat power spectral density (PSD) over the bandwidth between 5 and 20 Hz. An example of the resulting acceleration PSD is shown in FIGURE 8.

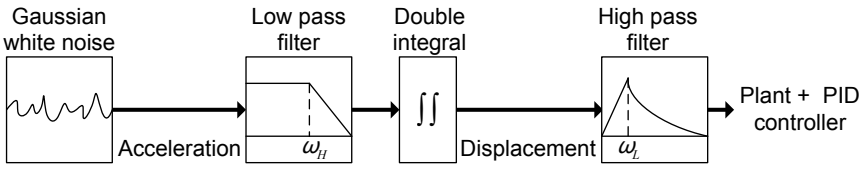

Figure 7: Obtaining a band limited white acceleration using position control.

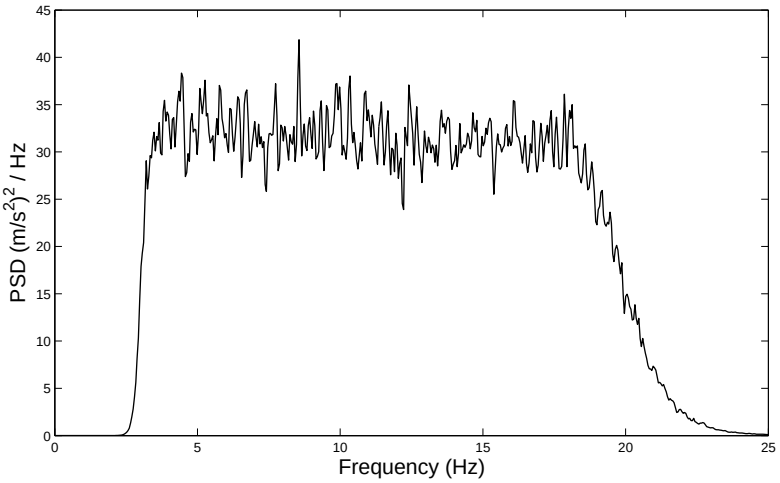

Figure 8: Example of base acceleration spectrum taken over 20 averages where the root mean square acceleration was 1.54 m/s^2.

5 PARAMETER IDENTIFICATION

Before the simulation could be validated against the experimental data all of the parameters in the equation of motion had to be identified for the time domain system.

5.1 Self Adaptive Differential Evolution

The mass of the centre magnet was easily measured while the other parameters (k, k_3, F_d, c) were identified using a Differential Evolution (DE) algorithm. The model was excited with the same signal that had been used to excite the real device and the algorithm was used to identify parameter values that would minimise the difference between the simulation and experiment time histories. Throughout this work, a self-adaptive differential evolution (SADE) algorithm was used. Details of this algorithm are described by Worden and Manson (2010).

5.2 Cost Function

A cost function was used to describe the level of similarity between the time response of the model and the experiment. This is shown in EQUATION 29:

$$J(c, F_d, k, k_3) = \frac{100}{N\sigma_z^2} \sum_{n=1}^{N} (z_n - \hat{z}_n(c, F_d, k, k_3))^2, \tag{29}$$

where n represents the point in the time history vector, z_n and σ_z^2 represent the time history and variance of the experimentally obtained relative displacement respectively, $\hat{z}_n$ represents the relative displacement according to the simulation and c, F_d, k and k_3 are the parameters to be identified. The cost function is such that if the model simply produced the mean of the experimental result (denoted $\bar{z}$) then the function will return a value of 100:

$$J(c, F_d, k, k_3) = \frac{100}{N\sigma_z^2} \sum_{n=1}^{N} (z_n - \bar{z})^2 = 100. \tag{30}$$

From experience it is known that a cost of less than five represents a good correlation, and that less than one can be considered excellent.

6 MODEL VALIDATION

Experiments were conducted under nine different conditions where each condition represented a different intensity of white noise excitation. The root mean square (RMS) value of each excitation signal and its corresponding condition is shown in TABLE 1. Each test was run long enough for the statistical moments of the relative displacement to converge. It was found that sixty seconds of testing was ample time for this to occur. To obtain the relevant parameters the SADE algorithm was run for 200 generations using the data from condition 1 as the training data. The identified parameters were then used to compare the response of the model with that of the experiment in all the noise conditions investigated. It was found that the model was able to accurately replicate the response of the experiment in the time and frequency domains for all the excitation intensities. Examples of this for conditions 2, 5 and 8 are shown in FIGURES 9, 10 and 11 respectively. It should be noted that the power output of the device was calculated according to EQUATION 10. The value of the cost function corresponding to each condition is also shown in TABLE 1. The identified parameter values are shown in TABLE 2.

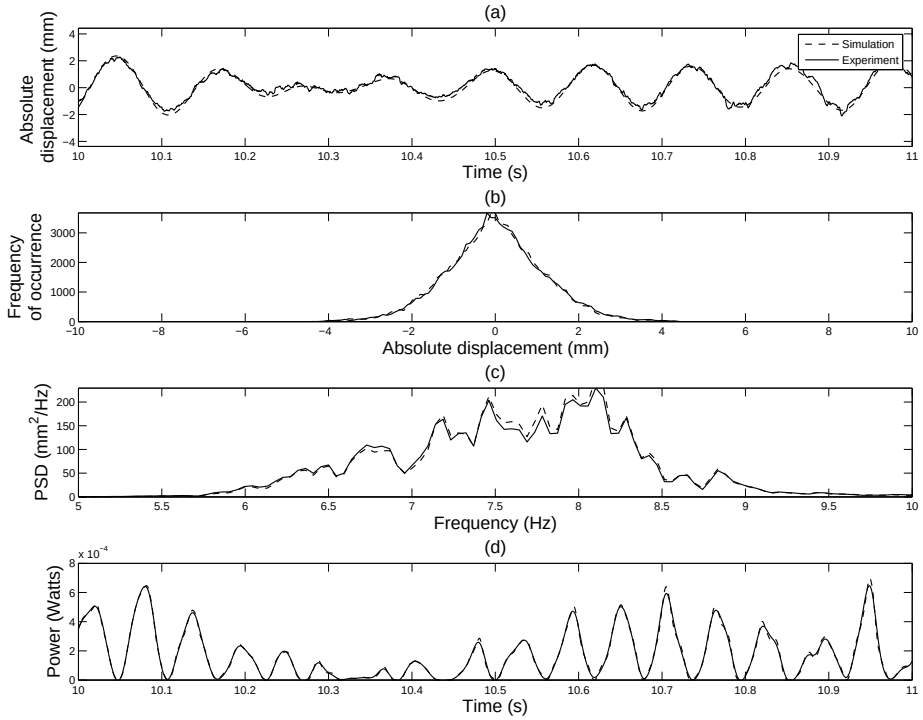

Figure 9: Comparison of simulation and experimental results for condition 2. Shown is centre magnet displacement (a) time history portion, (b) histogram,(c) frequency content and (d) device power output. Dashed lines and solid lines represent the simulation and experiment respectively. Model response was determined via numerical solutions of equations 3 and 4 using the fourth order Runge-Kutta method.

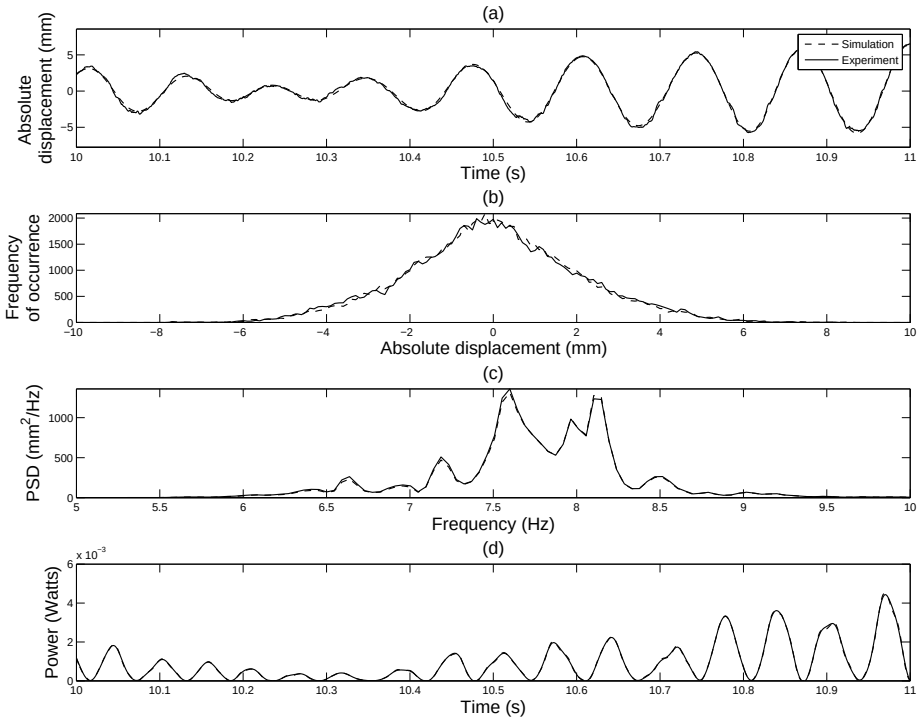

Figure 10: Comparison of simulation and experimental results for condition 5. Shown is centre magnet displacement (a) time history portion, (b) histogram,(c) frequency content and (d) device power output. Dashed lines and solid lines represent the simulation and experiment respectively. Model response was determined via numerical solutions of equations 3 and 4 using the fourth order Runge-Kutta method.

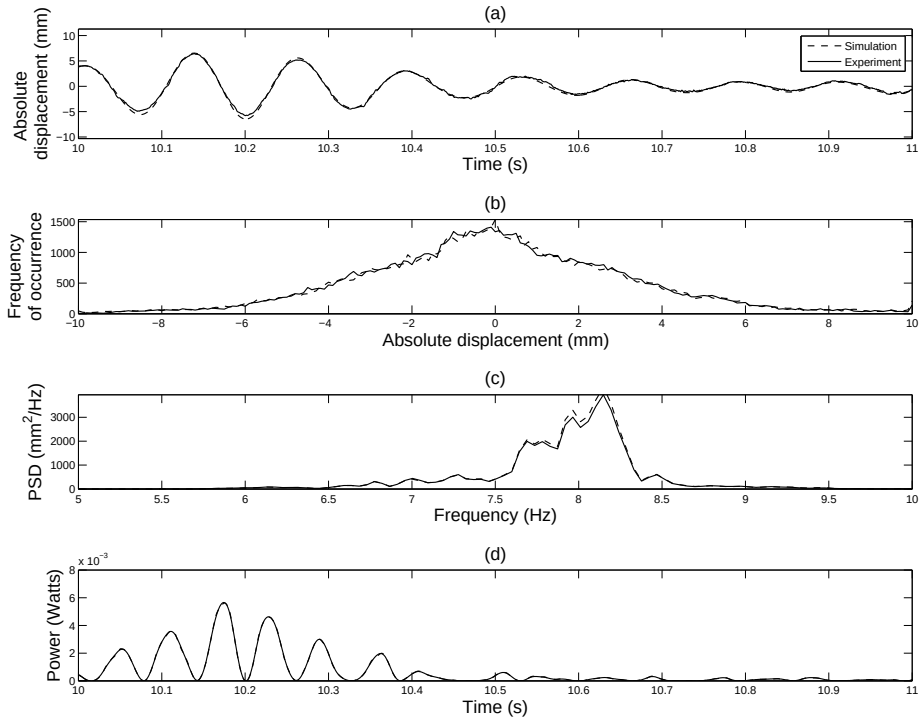

Figure 11: Comparison of simulation and experimental results for condition 8. Shown is centre magnet displacement (a) time history portion, (b) histogram,(c) frequency content and (d) device power output. Dashed lines and solid lines represent the simulation and experiment respectively. Model response was determined via numerical solutions of equations 3 and 4 using the fourth order Runge-Kutta method.

To ensure that the estimated parameter values were sensible, the stepped up and stepped down frequency response of the simulation was compared with that of the experiment. This was obtained using a stepped sine technique, where the root-mean-square (RMS) of the response amplitude was measured at each frequency. FIGURE 12 shows that there is good match between the frequency response of the real device and that of the model. It also shows that the model is able to demonstrate the jump phenomenon that is commonly associated with the hardening spring Duffing oscillator.

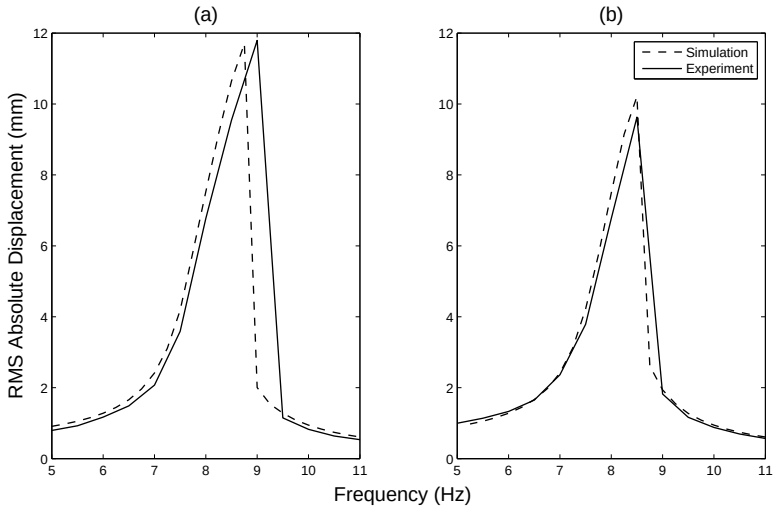

Figure 12: Comparison of (a) stepped up and (b) stepped down frequency response with an input amplitude of 0.8mm. Dashed lines and solid lines represent the simulation and experiment respectively. Exciting the model with a stepped-sine wave, the forth order Runge-Kutta method was used to numerically solve equations 3 and 4 thus obtaining the frequency response of the device.

7 WHITE NOISE BASE EXCITATION

Once the model was validated it was used to explore how the device would respond to a broadband white noise base excitation when different levels of nonlinearity, viscous damping and friction were present in the system. In this section it was assumed that all of the viscous damping was due to the electromagnetic coupling using the theory outlined in Section 2.2. This approach therefore predicts the maximum theoretical power that could be harvested from the device.

7.1 Dimensional Analysis

To begin the analysis, dimensionless groups corresponding to the power output, viscous damping, nonlinear stiffness and coulomb damping of the device were formed. Firstly, it was assumed that the power output of the device was a function of the following variables:

$$\sigma_P = f(\sigma_{\ddot{y}}, m, c, k, k_3, F_d), \tag{31}$$

where σ_P is the RMS power available from the device, $\sigma_{\ddot{y}}$ is the RMS acceleration of the base, m is the mass of the central magnet, c represents the damping in the system due to electromagnetic coupling, k and k_3 are the linear and nonlinear stiffness terms respectively and F_d is the coulomb damping coefficient. The primary variables chosen were base acceleration, mass and linear stiffness where

$$[\sigma_{\ddot{y}}] = LT^{-2}, \tag{32}$$

$$[m] = M, \tag{33}$$

$$[k] = MT^{-2}. \tag{34}$$

The first dimensionless group was found using the power term:

$$\pi_P = \sigma_P \sigma_{\ddot{y}}^{a_1} m^{a_2} k^{a_3}, \tag{35}$$

$$[\pi_P] = M^{1+a_2+a_3} L^{2+a_1} T^{-3-2a_1-2a_3} = 1, \tag{36}$$

which leads to the relationship:

$$\pi_P = \frac{\sigma_P \omega_n}{\sigma_{\ddot{y}}^2 m}. \tag{37}$$

The second dimensionless group was found using the damping term:

$$\pi_c = c\sigma_{\ddot{y}}^{a_1} m^{a_2} k^{a_3}, \tag{38}$$

$$[\pi_c] = M^{1+a_2+a_3} L^{a_1} T^{-1-2a_1-2a_3} = 1, \tag{39}$$

which leads to the relationship:

$$\pi_c = \frac{c}{\sqrt{km}}. \tag{40}$$

It is noted here that this group is the same as double the damping ratio that one finds in a linear mass-spring-damper system. The third dimensionless group was found using the nonlinear stiffness term:

$$\pi_{k_3} = k_3 \sigma_{\ddot{y}}^{a_1} m^{a_2} k^{a_3}, \tag{41}$$

$$[\pi_{k_3}] = M^{1+a_2+a_3} L^{-2+a_1} T^{-2-2a_1-2a_3} = 1, \tag{42}$$

which leads to the relationship:

$$\pi_{k_3} = \frac{k_3 \sigma_{\ddot{y}}^2 m^2}{k^3}. \tag{43}$$

The final dimensionless group was found using the coulomb damping term:

$$\pi_{F_d} = F_d \sigma_{\ddot{y}}^{a_1} m^{a_2} k^{a_3}, \tag{44}$$

$$[\pi_{F_d}] = M^{1+a_2+a_3} L^{1+a_1} T^{-2-2a_1-2a_3} = 1, \tag{45}$$

which leads to the relationship:

$$\pi_{F_d} = \frac{F_d}{\sigma_{\ddot{y}} m}. \tag{46}$$

As a result, one is left with four dimensionless groups, each one containing one of the parameters being investigated.

7.2 Results

Initially, it was assumed that there was no friction present in the simulated system. Monte Carlo simulations were run using a band-limited white noise force applied to the base of the device. This was done for different values of nonlinear stiffness and linear damping. It was ensured that the simulation results were independent of the simulation run time and sampling frequency. The dimensionless form of the results are shown in FIGURE 13 where the circles represent excitation conditions where the model was validated, as defined in TABLE 1. The simulation results suggest that the introduction of the spring nonlinearity into the system has no effect on its power output. It also seems to indicate a threshold value of damping ratio, above which, the power output of the system does not increase.

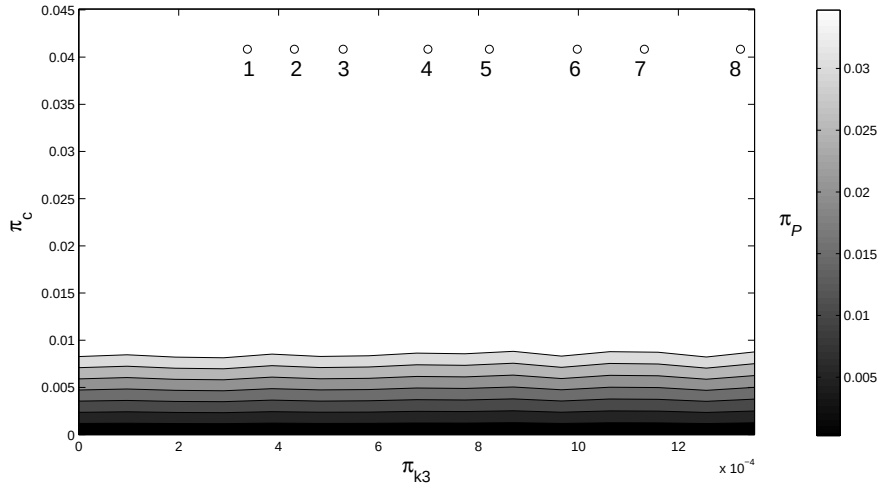

Figure 13: The variation of power output as k_3 and c are varied according to simulation results. Circles represent points where the model was validated while the values next to them represent the corresponding excitation condition. Model response was determined via numerical solutions of equations 3 and 4 using the fourth order Runge-Kutta method.

Having established that the nonlinear spring term does not affect the power output of the system, k_3 was set to zero and Monte Carlo simulations were used to investigate the relation between friction, damping and power output. The resulting contour plot is shown in FIGURE 14. It can clearly be seen that increased coulomb damping has a detrimental effect on the power output of the device. It is also clear that the harmful effect of friction can be reduced in most cases by increasing the electromagnetic coupling of the device. For the purposes of validation, it was ensured that the results demonstrated in FIGURE 14 were independent of values of k_3.

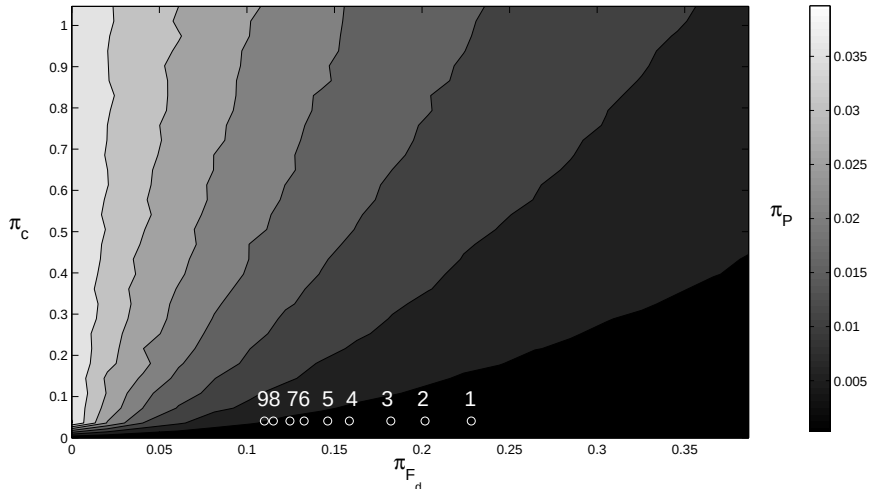

Figure 14: The variation of power output as F_d and c are varied according to simulation results where circles represent points where the model was validated. Model response was determined via numerical solutions of equations 3 and 4 using the fourth order Runge-Kutta method.

8 COLOURED NOISE BASE EXCITATION

With the model validated under white noise excitation conditions, it was then used to analyse the response of the device to coloured noise excitations.

8.1 Signal Generation

To generate the coloured noise base acceleration, a white noise signal was passed through a second order filter such that:

$$\ddot{y} + 2\omega_c \alpha \dot{y} + \omega_c^2 y = W(t), \tag{47}$$

where $W(t)$ is white noise, ω_c is the natural frequency of the filter and α is the damping ratio of the filter.

8.2 Dimensional Analysis

It is now assumed that the RMS power output of the device is a function of the following variables:

$$\sigma_P = f(\sigma_{\ddot{y}}, m, c, k, k_3, F_d, \omega_c, \alpha) \tag{48}$$

Once again, the primary variables were chosen as $\sigma_{\ddot{y}}$, m and k. As a result, all the derived groups were the same as those shown in Section 7.1 except for the addition of two additional groups:

$$\pi_{\omega_c} = \frac{\omega_c m^{1/2}}{k^{1/2}}, \tag{49}$$

$$\pi_\alpha = \alpha. \tag{50}$$

It is noted that π_{ω_c} is the ratio of the filter and device linear natural frequencies and that, $\pi_\alpha = \alpha$ as α was already a dimensionless quantity.

8.3 Results

For the first set of Monte-Carlo simulations, π_c and π_α were held constant while π_{F_d} was set to zero. As a result, the value of π_P was monitored as the π_{k_3} and π_{ω_c} groups were varied. As one would expect, it was found that an increase in k_3 had the effect of shifting the natural frequency of the device to higher frequencies. FIGURE 15 demonstrates the effect of k_3 on a device which has been mistuned such that its natural frequency is lower than than of the dominant frequency of excitation ($\pi_{\omega_c} = 1.2$). In this scenario one can see that the increase in k_3 has shifted the natural frequency of the device closer to the dominant frequency of excitation and has, as a result, increased power output.

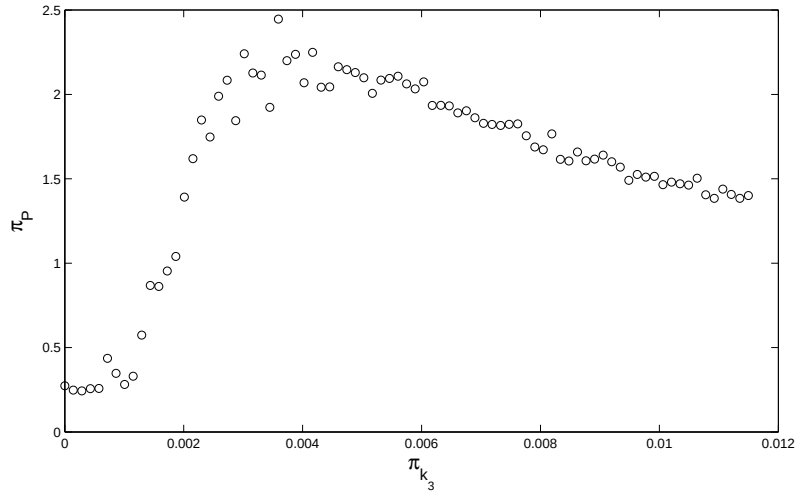

Figure 15: Variation of π_P as π_{k_3} is varied where $\pi_c = 0.03$, $\pi_{\omega_c} = 1.2$, $\pi_\alpha = 0.001$ and $\pi_{F_d} = 0$. Model response was determined via numerical solutions of equations 3 and 4 using the fourth order Runge-Kutta method.

For the second set of simulations, π_{k_3} was set zero and π_{ω_c} was set equal to one such that the response of a linear device which has been tuned to the dominant frequency of excitation was being modelled. FIGURES 16 (a) and (b) show how π_P was effected by changes in π_c and π_{F_d} for different values of π_α. Aside from showing that friction is detrimental to the power output of the device, the simulation results appear to show that the system's sensitivity to changes in damping is dependent on the excitation type. For example, in FIGURE 16 (a) (where a low value of π_α was chosen) one can clearly see that the a low value of damping is desirable. However, as π_α is increased and the signal becomes more alike to broadband white noise then changing damping has less effect on power output (FIGURE 16 (b)) and the behavior starts to approach that shown in FIGURE 14.

Finally, π_{k_3} was set to zero, π_α was held at 0.2 and simulations were run to investigate the effect of changing π_c and π_{F_d} for different values of π_{ω_c}. By changing π_{ω_c} one was able to study how the response of the device responded to different levels of mistuning (where the natural frequency of the device differs from the dominant frequency of excitation). FIGURE 16 (c) shows simulation results for the case where $\pi_{\omega_c} = 1.3$. One can see that the mistuning has reduced the maximum power output of the device as well as increasing the optimum level of viscous damping. This is likely due to the fact that larger levels of viscous damping widen the useful bandwidth of the device. Consequently, when the device is mistuned the increase in damping is desirable as it helps to extend the useful bandwidth of the device into the dominant frequencies of excitation.

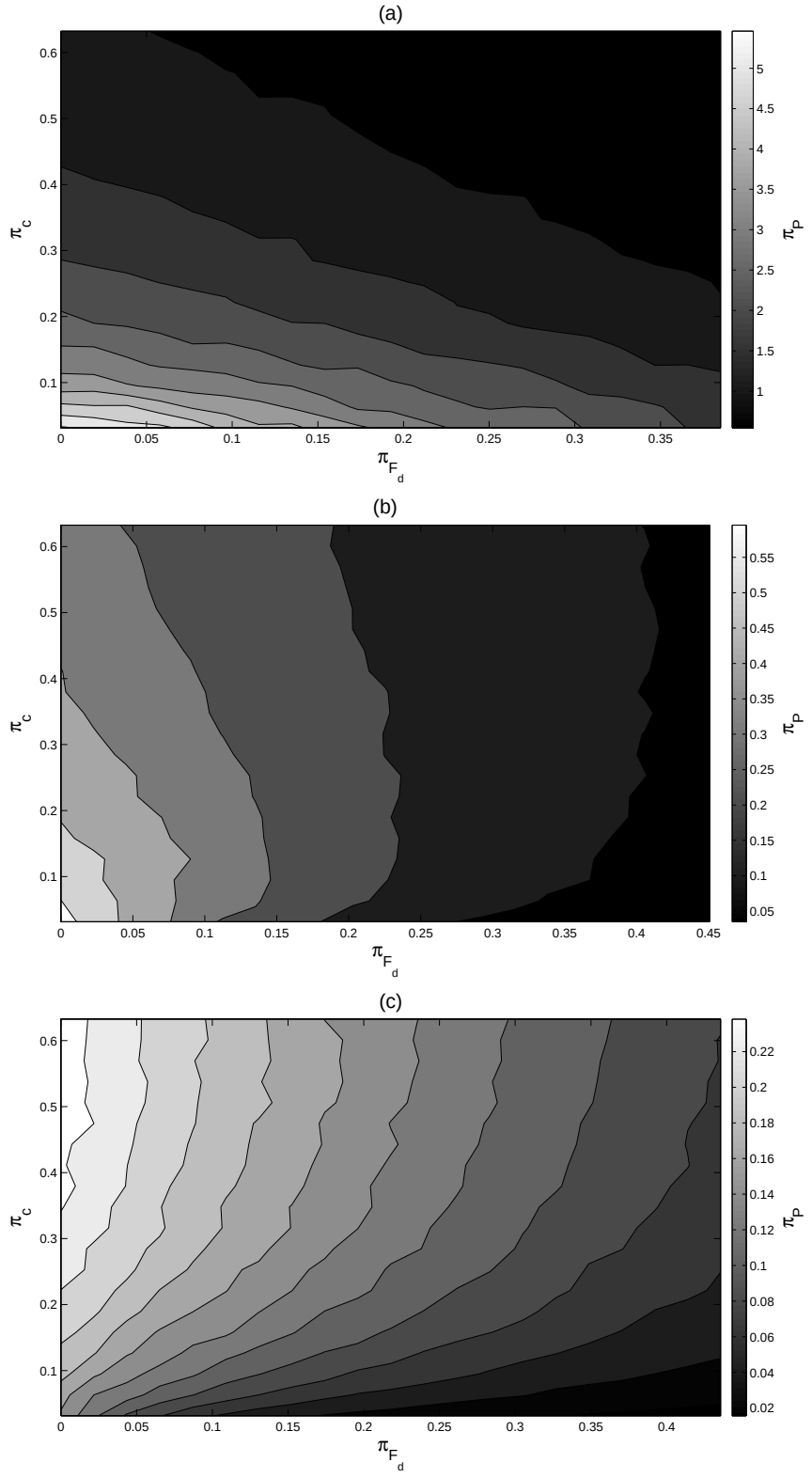

Figure 16: Variation of π_P as π_c and π_{F_d} is varied where $\pi_{k_3} = 0$ and (a) $\pi_{\omega_c} = 1$, $\pi_\alpha = 0.05$, (b) $\pi_{\omega_c} = 1$, $\pi_\alpha = 0.2$, (c) $\pi_{\omega_c} = 1.3$, $\pi_\alpha = 0.2$. Model response was determined via numerical solutions of equations 3 and 4 using the fourth order Runge-Kutta method.

9 DISCUSSION

A number of issues are worthy of further discussion. The experiments did not involve energy capture and all losses were due to viscous and Coulomb damping. However, in Section 2.2 it was explained how a simplified model of electromagnetic coupling allows the harvesting to be represented by the mechanical analogy of a viscous damper (EQUATION 10). Meanwhile, a dimensionless approach has been used in the interpretation of the performance, which remains valid if this simple electromagnetic coupling is present. Consequently the present work is useful for illustrating the maximum possible energy that could be harvested from a real device if mechanical and electrical losses were negligible. Nevertheless, further work is clearly needed to understand the role of energy capture, and any associated nonlinearities, in more detail.

A key finding from this work is that, when under a broadband excitation, Duffing-type nonlinearities cannot be used to improve device power output. With regards to coloured noise excitations, it was shown that Duffing-type nonlinearities may prove useful in a scenario where one needed to tune the natural frequency of the device to a higher value without changing the mass or linear stiffness terms. It should also be noted that if the kinetic energy losses present in the device were too high or the excitation level too low then the level of nonlinearity required to shift the natural frequency may be too high to be achieved practically. Additionally, although coloured noise excitations are regarded as a better approximation of ambient vibrations than sinusoidal or broadband excitations, future work could be directed at more specific cases. This is further emphasised by the results shown in Section 8.3 which shows that the optimum level of electrical damping for such a device is dependent on the excitation type and the likelihood of device mistuning.

Finally, for all the excitation types investigated, the detrimental effects of friction were demonstrated. The investigation of friction is likely to be significant for many practical applications where energy capture involves electromagnetic, rather than piezoelectric phenomenon, since electrical machines will generally require mechanical bearings.

10 CONCLUSIONS

In this work, an energy harvesting device with Duffing-type and Coulomb damping nonlinearities is analysed. Firstly, the response of the device to a sinusoidal excitation is analysed using the method of harmonic balance. As well as showing that the DC components and super-harmonic components of the response do not have a great effect on power output, an expression was derived which can be used to determine whether the centre magnet of the device will be able to overcome friction present in the system.

Secondly, by approximating the magnetic levitation force-displacement relationship by using a cubic polynomial, it was found that the resulting model was able to match the response of the experiment excellently, regardless of the excitation intensity. This resulted in a high fidelity model despite the simplified modelling of the permanent magnet restoring forces.

Thirdly, the parameters governing the power output of the device were non-dimensionalised such that the findings from this paper apply to all devices of this sort. It was also found that the dimensionless group which contained the nonlinear spring term also contained a term representing the RMS base acceleration. Experimentally, this allowed the effect of different levels of nonlinearity to be formally studied by varying the intensity of the base excitation, rather than attempting to modify the nonlinearity directly.

Fourthly, the validated model was used to analyse the response of the device to broad band white noise and excitations. It was found that the Duffing-type nonlinearities had no effect on the power output of the device. It was also shown that the effect of changes in damping on device performance are altered when friction is included in the system.

Finally, the model was used to analyse the response of the device to coloured noise excitations. It was shown that Duffing-type nonlinearities could be used to tune the natural frequency of the device to higher frequencies without having to change the mass or linear stiffness of the system. As a result, it can be

concluded that the one scenario where the nonlinearity could be used to improve the power output of the device is when its linear natural frequency is lower than the dominant frequency of excitation. Additionally, it was shown that the affect of damping on the system performance is dependent on the type of excitation as well as the level of friction present in the device. Due to the increased useful bandwidth that one can achieve with high levels of damping, it is suggested that the optimum level of damping for such a device should be chosen depending on the likelihood that the device will be mistuned with respect to the dominant frequency of excitation. This will be especially important if one were to consider ambient vibrations which possess dominant frequencies that are time dependent.

ACKNOWLEDGEMENTS

The authors would like thank Les Morton for his technical assistance and to acknowledge support from an EPSRC studentship, grant reference EP/H020764/1.

References

Beeby, S.P., Tudor, M.J., and White, N.M., 2006. "Energy harvesting vibration sources for microsystems applications." Measurement Science and Technology, 17(12):R175.

Daqaq, M.F., 2010. "Response of uni-modal duffing-type harvesters to random forced excitations." Journal of Sound and Vibration, 329(18):3621–3631.
Daqaq, M.F., 2011. "Transduction of a bistable inductive generator driven by white and exponentially correlated Gaussian noise." Journal of Sound and Vibration, 330(11):2554 – 2564.

Mann, B.P. and Sims, N.D., 2009. "Energy harvesting from the nonlinear oscillations of magnetic levitation." Journal of Sound and Vibration, 319(1-2):515–530.

Mann, B.P. and Sims, N.D., 2010. "On the performance and resonant frequency of electromagnetic induction energy harvesters." Journal of Sound and Vibration, 329(9):1348–1361.

MathWorks., 2004. "roots." Matlab Help Files.

Mitcheson, P., Green, T., Yeatman, E., and Holmes, A., 2004. "Architectures for vibration-driven micropower generators." Journal of Microelectromechanical Systems, 13(3):429–440.

Sneller, A. and Mann, B., 2010. "On the nonlinear electromagnetic coupling between a coil and an oscillating magnet." Journal of Physics D: Applied Physics, 43(29). Cited By (since 1996) 0.

Stephen, N., 2006. "On energy harvesting from ambient vibration." Journal of Sound and Vibration, 293(1-2):409 – 425.
Tang, L., Yang, Y., and Soh, C., 2010. "Toward broadband vibration-based energy harvesting." Journal of Intelligent Material Systems and Structures, 21(18):1867–1897.

Williams, C.B. and Yates, R.B., 1996. "Analysis of a micro-electric generator for microsystems." Sensors and Actuators A: Physical, 52(1-3):8 – 11. Proceedings of the 8th International Conference on Solid-State Sensors and Actuators Eurosensors IX.

Worden, K. and Manson, G., 2010. "On the identification of hysteretic systems, Part I: an extended evolutionary scheme." Proceedings of IMAC XVIII, Conference and Exposition on Structural Dynamics, Jacksonville, Florida.

Yang, Bin, Lee, Chengkuo, Xiang, Wenfeng, Xie, Jin, He, Han, J., Kotlanka, Krishna, R., Low, Ping, S., and Feng, H., 2009. "Electromagnetic energy harvesting from vibrations of multiple frequencies." Journal of Micromechanics and Microengineering, 19(3).

Zhu, D., Tudor, M.J., and Beeby, S.P., 2010. "Strategies for increasing the operating frequency range of vibration energy harvesters: a review." Measurement Science & Technology, 21(2).

Table 1: RMS and associated cost for each excitation condition where condition 1 was used as the training data.

	Excitation Condition	RMS (m/s^2)	Cost
Training Data Set	1	1.07	2.71
Validation Data Sets	2	1.21	4.09
	3	1.34	1.98
	4	1.54	2.07
	5	1.67	1.31
	6	1.84	1.57
	7	1.96	1.60
	8	2.12	0.99
	9	2.22	1.57

Table 2: Parameter values identified using the SADE algorithm

Parameter	Value	Units
c	0.048	Ns/m
F_d	0.006	N
k	56.2	N/m
k_3	86579	N/m^3